Check for updates

# Controllable synthesis of hollow spherical nickel chalcogenide (NiS₂ and NiSe₂) decorated with graphene for efficient supercapacitor electrodes†

Min Lu,*[a] Ming-yuan Sun,[a] Xiao-hui Guan, [ID][a] Xue-mei Chen*[a] and Guang-Sheng Wang [ID]*[b]

New carbon-loaded nickel chalcogenide electrode materials (NiS₂/GO and NiSe₂/rGO) have been synthesized through an easy-to-operate process: NiSe₂ was obtained based on NiS₂ hollow spheres, and was successfully synthesized with L-cysteine assistance under the hydrothermal method at 120 °C. GO of different mass fraction was added together with L-cysteine. The electrochemical performance of NiS₂/GO and NiSe₂/rGO has been greatly improved because the formation of a carbon-loaded layer effectively increased the specific surface area and reduced the charge transport resistance. Compared with pure NiS₂ and NiSe₂, NiS₂/GO and NiSe₂/rGO presented much better specific capacitance (1020 F $g^{-1}$ and 722 F $g^{-1}$ respectively at a current density of 1 A $g^{-1}$) and more superior rate capability (when the current density was raised to 5 A $g^{-1}$ the specific capacitance remained at 569 F $g^{-1}$ and 302 F $g^{-1}$). This work highlights the advantages of nickel compounds through a very simple experimental method, and contributes to providing a good reference for preparation of superior supercapacitor materials with high performance.

## 1 Introduction

With the decline of fossil energy, there has been a positive exploitation of alternative energy sources and high efficiency energy storage devices.[1,2] Supercapacitors (SCs),[3,4] also called ultracapacitors or electrochemical capacitors, store electrical charge on high-surface-area conducting materials. As new energy storage components, SCs are different from traditional capacitors and batteries because of their advantages, including high power density, high specific capacity, quick charge and discharge, long cycle life and high safety capacity.[5–9] Therefore, SCs have a good application prospect in the fields of high-power and high-energy power supply, clean energy, smart grid, transportation, wireless communication, aerospace, military, electronic equipment and so on. However, the relatively low energy density of supercapacitors seriously limits their commercial application.[10,11] At present, research teams at home and abroad mainly develop new electrode materials, electrolytes and asymmetric super capacitors to maintain high power density

and cycle stability of energy storage device and further improve the properties.

As we all know, electrode materials, as the core component of the device, play a decisive role in the development and commercial application of supercapacitors. Moreover, their composition, morphology and structure have a crucial impact on the electrochemical performance of the materials in the design of electrode materials.[12–14] Nanostructured transition metal chalcogenide, as electrode materials, are considered to be inorganic functional materials with application prospects due to the charge storage through Faraday reaction of metal ions.[15] Nevertheless, a series of single nanomaterials with different compositions and morphologies, have mostly been explored at the research level as pseudo capacitors (PCs) electrode materials in labs rather than at the industrial level for practical application, due to their rapid degradation and low capacity retention in high reversible ion adsorption or rapid redox reactions.[16] For instance, Pang *etc.* prepared nickel oxide nanostructures with different lengths and NiO nanowires with the longest length have the largest specific capacitance of 180 F $g^{-1}$.[17] Sun *etc.* prepared NiS₂ nanospheres *via* a facile one-step polyvinylpyrrolidone assisted method which delivers a high reversible specific capacity of 692 mA h $g^{-1}$.[18] Mondal *etc.* produced porous NiCo₂O₄ hollow spheres which showed specific capacity as high as 183 C $g^{-1}$.[19] Li *etc.* prepared graphene/NiS₂ composite through a template-free solvothermal reaction using graphene oxide shows a great value of 478.1 F $g^{-1}$ at a current density of 0.5 A $g^{-1}$.[20] However, it is noteworthy that the hollow spheres

[a]School of Chemical Engineering, Northeast Electric Power University, Jilin 132000, P. R. China

[b]Key Laboratory of Bio-Inspired Smart Interfacial Science and Technology of Ministry of Education, School of Chemistry, Beihang University, Beijing 100191, P. R. China. E-mail: wanggsh@buaa.edu.cn

† Electronic supplementary information (ESI) available. See DOI: 10.1039/d0ra10659c

sulfides with the large internal space are more likely showing excellent physical and chemical properties such as low density, large effective area and good mass permeability to have more active sites and faster charge transfer ability and further improve the electrochemical properties of materials.[21,22]

Compared with single nickel chalcogenide, nanocomposites can make full use of the synergistic and complementary effects among components, which makes them have greater advantages in application.[23–25] Among them, for the carbon based transition metal compound composite, the introduction of carbon material can improve the overall conductivity of the material on the one hand, and effectively inhibit the agglomeration of small-size active substances, so that the composite has a larger specific surface area, fully contact with the electrolyte, thus improving its charge transfer and storage capacity.[26,27] On the other hand, the excellent structure and chemical stability of carbon materials can buffer the volume change of materials during charging and discharging, and improve the cyclic stability of materials.[28–30] When nickel sulfides/graphene composites are used as pseudocapacitor electrode materials, the graphene can not only provide an elastic space to buffer the volume change of the electrode materials during the repetitive charge/discharge process, but also facilitate the faster electron transport, resulting in an enhanced electrochemical performance.[31,32] It has been demonstrated that the solvothermal synthesized NiS/graphene composite[33,34] and $Ni_3S_2$/N-doped graphene composite[35] exhibited the enhanced electrochemical performances in comparison with the NiS and $Ni_3S_2$. In particular, when combined with graphene, the specific capacitance of NiO increased from 47.2 F g$^{-1}$ to 187.53 F g$^{-1}$ at 10 mV s$^{-1}$ scan rate. And the discharge–charge cycling stability of the $Ni_3S_2$@N-G and bare $Ni_3S_2$ was examined at a current density of 50 mA g$^{-1}$ between 0.01 and 3.0 V delivers initial discharge–charge capacities of 1739 and 729 mA h g$^{-1}$ respectively.

Herein, in this work, we prepared a series of controllable morphology hollow spheres $NiS_2$ and microspheres $NiSe_2$ composited with graphene by a simple and effective hydrothermal process by adjusting the graphene oxide concentration, and the result composites were characterized by XRD (X-ray diffraction pattern), SEM (scanning electron microscopy), FTIR (Fourier transformed infrared spectroscopy), TG (thermogravimetric analysis) and XPS (X-ray photoelectron spectroscopy). The electrochemical performances of $NiS_2$/graphene oxide (GO) composite and $NiSe_2$/reduced graphene oxide (rGO) composite were furtherly researched and compared in detail based on cyclic voltammetry (CV), galvanostatic charge–discharge (GCD) and electrochemical impedance spectroscopy (EIS) techniques.

## 2 Experimental

### 2.1 Sample preparation

**2.1.1 Preparation of graphene oxides.** Graphene oxides (GO) were synthesized *via* a modified Hummers method using pristine graphite powders as raw materials. The detail procedure are described in ESI.†

**2.1.2 Preparation of $NiS_2$ and $NiS_2$/GO hollow spheres.** All of the chemicals are analytical grade and used without further purification. In a typical synthesis,[36] 1 mmol Ni(NO$_3$)$_2$·6H$_2$O and 1 mmol urea were dissolved in 20 mL of deionized water with magnetic stirring, then 4 mmol L-cysteine and 50 mL deionized water were added. L-Cysteine is the source of sulfur. After ultrasonic treatment, the homogeneous suspension was transferred into a 100 mL teflon-lined stainless steel autoclave for solvothermal reaction at 120 °C for 24 h. The black precipitates of hollow spherical $NiS_2$ were washed several times with distilled water and absolute ethanol and dried at 60 °C for 12 h for further characterization. To obtain $NiS_2$/GO nanocomposites, GO of ten percent (10 wt%), fifteen percent (15 wt%), twenty percent (20 wt%), twenty five percent (25 wt%) and thirty percent (30 wt%) was added to the above mixed solvent together with 4 mmol L-cysteine. To distribute GO evenly in the solution, an additional stirring time of 30 minutes was added. The following processing steps are consistent with the method used to prepare $NiS_2$.

**2.1.3 Preparation of $NiSe_2$ and $NiSe_2$/rGO hollow spheres.** The 1 mmol above-prepared hollow spherical $NiS_2$ was stably dispersed in 40 mL of deionized water under magnetic stirring. 2 mmol H$_2$SeO$_3$ and 5 mL of N$_2$H$_4$·H$_2$O were added in this solution, and transferred to a 100 mL teflon-lined stainless steel autoclave and heated at 140 °C for 24 h, then the solution was cooled to room temperature. The products of $NiSe_2$ were obtained after washing and drying. In composite preparation, GO of one percent (1 wt%), three percent (3 wt%), five percent (5 wt%) and seven percent (7 wt%) was added to the above mixed solvent together with N$_2$H$_4$·H$_2$O. The following processing steps are consistent with the method used to prepare $NiSe_2$ except the addition of graphite oxide.

### 2.2 Characterization

The morphology and size of the products were obtained using scanning electron microscopy (SEM) with a JSM-6510A microscope and by sputtering with gold. The samples were examined by X-ray diffraction (XRD-7000), recorded using a Shimadzu X-ray powder diffractometer with Cu-Kα radiation ($\lambda$ = 0.15405 nm). X-ray photoelectron spectroscopy (XPS, ESCALAB-250) with an Al-Kα radiation source were used. Chemical bonding information of the studied samples was gathered with Fourier transformed infrared spectroscopy (FTIR, Nicolet iS50). Thermogravimetric analysis (TG) was carried out using MettlerToledo TGA/DSC1 apparatus.

### 2.3 Test of electrochemical properties

The electrochemical properties of the prepared-samples were tested by an electrochemical workstation (Parstat 4000) under a conventional three-electrode system in the electrolyte of 2.0 M KOH aqueous solution (*i.e.* a saturated Hg/HgO reference electrode, a platinum counter electrode and a working electrode). Among them, the working electrode was prepared using the active materials by the following procedure: the prepared active material, acetylene black and a polytetrafluoroethylene (PTFE) emulsion were mixed in ethanol with a weight ratio of 8 : 1 : 1;

the slurry was coated on a nickel foam ($1.0 \times 1.0$ cm$^2$) current collector and then pressed at 8 MPa for 30 s, and dried under vacuum at 60 °C for 12 h. Finally, the mass of the active loading on the nickel foam was about 10 mg. The average specific capacitance of the electrodes was calculated by eqn (1) based on the cyclic voltammogram curves.

$$C = \frac{\int_{V_0}^{V} I(V)\mathrm{d}V}{mv(V-V_0)} \quad (1)$$

where $C$ (F g$^{-1}$), $m$ (g), $v$ (V s$^{-1}$), $V–V_0$ (V), and $I$ (V) are the specific capacitance, mass of the active material on the working electrode, potential scan rate, potential range and current density, respectively. Besides, based on the galvanostatic charge–discharge curves, the average specific capacitance of the electrodes was calculated according to eqn (2).

$$C_S = \frac{I \times \Delta t}{\Delta V \times m} \quad (2)$$

where $C_S$ (F g$^{-1}$), $I$ (A), $\Delta t$ (s) and $\Delta V$ (V) are the specific capacitance, discharge current, discharge time and potential range of discharge, respectively.

## 3 Results and discussion

### 3.1 Morphology and structure analysis of samples

As well shown in Fig. 1a and b, as-synthesized NiS$_2$ and NiSe$_2$ are of hollow spherical structure, which are consistent with our previous report.[37] And the diameters of these hollow spheres are approximately 2.33 μm. After introducing GO (percentage content like 20% and 3% was the amount of graphene oxide added in the preparation process), from Fig. 1c and S1,† it was found that nickel chalcogenides NiS$_2$ coated by GO still retains the hollow spherical structure. Meanwhile, the NiS$_2$ hollow spheres could effectively avoid agglomeration of GO nanosheets. The crinkled and flexible GO surface is beneficial to increasing interface areas between GO sheets and NiS$_2$ hollow spheres. Due to the addition of hydrazine hydrate in the synthesis process of NiSe$_2$, the GO was chemically reduced to

rGO. Fig. 1d and S2† show the corresponding SEM image of NiSe$_2$ decorated with rGO. It can be noticed that the more graphene is introduced, the greater thickness of the nanosheets of rGO is. It can be concluded that nickel chalcogenides on the surface of the graphene sheets can be used as a separator, which could effectively prevent the aggregation of the spheres and the restacking of the graphene oxide sheet to a certain extent. However, with the increase of graphene oxide concentration, agglomeration becomes more and more serious, which is also one of the reasons for the decline of electrochemical performance.

To study the crystal structures of all samples, the XRD patterns have been provided in Fig. 2 and S3.† It shows XRD pattern of hollow spherical NiS$_2$ and the diffraction peaks at angles of 27.3°, 31.8°, 35.4°, 38.8°, 45.2°, 53.4°, 58.5°and 61.1° can be indexed to the (111), (200), (210), (211), (220), (311), (023), (321) planes, respectively, which is a pure cubic phase NiS$_2$ (JCPDS card no. 89-1495). The XRD pattern of NiSe$_2$ all the diffraction peaks can be indexed to the cubic phase NiSe$_2$ (JCPDS card no. 11-0552). Because of no peaks for other impurities in the above-mentioned XRD patterns, NiS$_2$ and NiSe$_2$ with the high purity and good crystallinity are synthesized under the current experimental conditions.[38] Moreover, the XRD patterns of nickel nanocomposites decorated with GO are almost the same as that of hollow spherical nickel chalcogenides (Fig. 2 and S3†). As we all known, the diffraction peak appears at $2\theta = 10.6°$ corresponding to the (001) plane of GO. Therefore, in theory the absence of the X-ray diffraction peak for GO around 10.6° in these nanocomposites indicates that GO can be reduced to rGO at $2\theta = 26.5°$ effectively. However, this characteristic peak of GO and rGO is not observed in the XRD pattern of both 20%-NiS$_2$/GO and 3%-NiSe$_2$/rGO. It may be that the strength of Ni peak is too high or the content of graphene is too less to observe the broad peak of rGO.[39]

Therefore, FT-IR spectrum was performed to certify the existence of graphene. As shown in Fig. S4,† the stretching vibration peak at 3400 cm$^{-1}$ for nanocomposites corresponds to the hydroxyl group. The peaks of 20%-NiS$_2$/GO at 1730 cm$^{-1}$ and 1644 cm$^{-1}$ are symmetric and antisymmetric stretching vibrations of carboxyl groups in GO. And the stretching vibration peak at 700 cm$^{-1}$ correspond to C–O and C–O–C also indicates the oxidation degree of graphite is ideal and it contains oxygen-containing functional groups. Nevertheless,
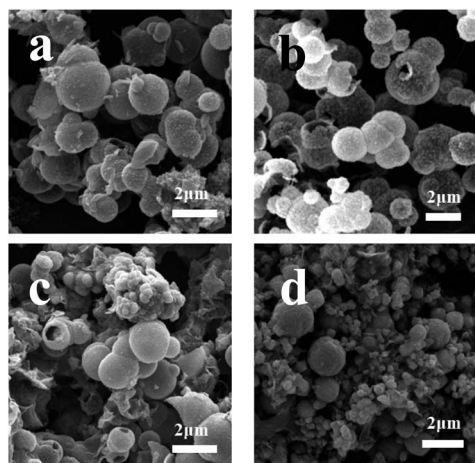


**Fig. 1** SEM images of as-prepared samples (a) NiS$_2$; (b) NiSe$_2$; (c) 20%-NiS$_2$/GO; (d) 3%-NiSe$_2$/rGO.
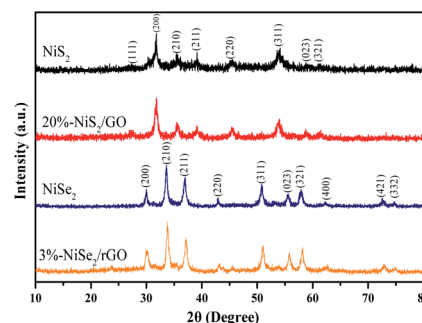


**Fig. 2** XRD patterns of the synthesized products.

most of the oxygen-containing functional groups in the 3%-NiSe$_2$/rGO prepared by hydrazine hydrate reduction disappeared and only a small amount of epoxy group existed, indicating that GO was reduced to rGO.

The surface elemental composition and chemical state of the nickel nanocomposites decorated with GO are investigated by X-ray photoelectron spectroscopy (XPS). The survey spectrum (Fig. S5a†) shows that the 20%-NiS$_2$/GO and 3%-NiSe$_2$/rGO are composed of Ni, O, C, S and Ni, O, C, Se elements, respectively, without other impurities. The high-resolution XPS spectrum of Ni 2p (Fig. S5b†) illustrates two shake-up satellites and two characteristic peaks, which can be assigned to Ni 2p$_{3/2}$ and Ni 2p$_{1/2}$ orbitals of Ni$^{2+}$. Furthermore, the spectrums of S 2p (Fig. S5c†) and Se 3d (Fig. S5d†) display the presence of $(S_2)^{2-}$ and Se$^{2-}$. In Fig. 3, it can be obviously found from the C 1s spectra that each of the two composite materials has five types of functional groups. Among them, 20%-NiS$_2$/GO has O–C=O (291 eV), C=O (288 eV), C–O (286.8 eV), sp$^3$ C–C (285.8 eV) and sp$^2$ C=C (284.5 eV), while 3%-NiSe$_2$/rGO has C=O (288.4 eV), C–O (285.9 eV), sp$^3$ C–C (284.8 eV), sp$^2$ C=C (284.2 eV) and C (graphite) (283.3 eV) respectively. Due to the existence of reducing agents during the synthesis of NiSe$_2$/rGO, the strength of the oxygen-containing functional groups (C=O and C–O) are significantly lower than that of NiS$_2$/GO, as indicates that a reduction process occurs.

The possible synthesis mechanism of the nickel chalcogenides decorated with GO is proceeded as follows (Scheme 1). Firstly, Ni(NO$_3$)$_2$ is used as the nickel source and L-cysteine is used as the sulfur source which provides a chemical chain mercaptan (–SH) with a strong tendency to coordinate with inorganic ions and form Ni$^{2+}$–L-cysteine complex. In this process, two complexes of Ni$^{2+}$–L-cysteine react to form the original nucleus of NiS$_2$. Urea provides an alkaline medium through hydrolysis during the self-assembly process. Meanwhile, GO can be added to synthesise the homologous composites by the common thermal treatment of the as-prepared NiS$_2$. While hollow spherical NiSe$_2$ is obtained by secondary hydrothermal process with a strong reductant N$_2$H$_4$·H$_2$O, leading to the reduction of Se$^{4+}$ and the substitution for S$^{2-}$. Then we add GO based on as-prepared NiS$_2$. In the hydrothermal process, hydrazine hydrate reduces Se$^{4+}$ to Se$^{2-}$ as well as GO to rGO.

The reaction route for the synthesis of NiS$_2$ could be expressed as the following chemical equations according to ref. 40 and [41]:
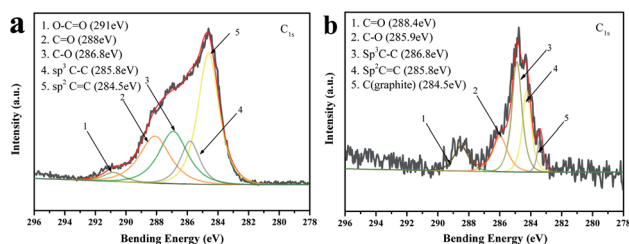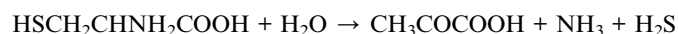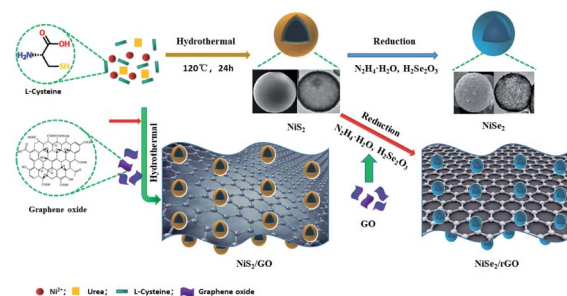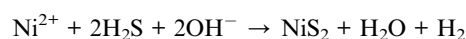
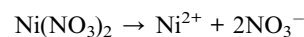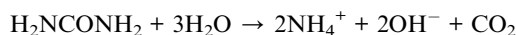$$HSCH_2CHNH_2COOH + H_2O \rightarrow CH_3COCOOH + NH_3 + H_2S$$



**Fig. 3**  XPS spectra for (a) C 1s of 20%-NiS$_2$/GO; (b) C 1s of 3%-NiSe$_2$/rGO.



**Scheme 1**  Schematic description of the synthetic process of NiS$_2$, NiSe$_2$ and their complexes.

$$H_2NCONH_2 + 3H_2O \rightarrow 2NH_4^+ + 2OH^- + CO_2$$

$$Ni(NO_3)_2 \rightarrow Ni^{2+} + 2NO_3^-$$

$$Ni^{2+} + 2H_2S + 2OH^- \rightarrow NiS_2 + H_2O + H_2$$

### 3.2  Electrochemical performances

The electrochemical properties of NiS$_2$, NiS$_2$/GO, NiSe$_2$ and NiSe$_2$/rGO were evaluated using CV and GCD techniques using a three-electrode cell in 2 M KOH aqueous electrolyte. Fig. S6 and S7† shows the typical CV curves of NiS$_2$/GO and NiSe$_2$/rGO at different scan rates with a potential window ranging from 0 V to 0.45 V, respectively. The CV measurements of NiS$_2$ and NiSe$_2$ were also carried out for comparison. In Fig. S6 and S7,† each pair of peaks are visible in each voltammogram. In the cathodic scanning, a small amount of charges would be storaged in the interphase between the electrode material and electrolyte, which occurs at different peaks. In the reverse anodic scanning, the stored charge would be released, which displays the different peaks. When the scan rate is increased, the shapes of the curves are maintained and the peaks current increase. The CV curves of all electrodes involving the reversible redox reactions are expected to exhibit good quasi-capacitance. We choose three different weight ratios of GO and rGO to highlight the differences of each electrode materials and the others are shown in ESI.† Fig. 4(a) and (b) show CV curves of NiS$_2$ and NiSe$_2$ compared with their composites with different weight ratios of rGO respectively at a scan rate of 10 mV s$^{-1}$, where the well symmetry of all CV curves implying the high rate capacity.[42] More importantly, form the larger integrated area of the CV curves means the higher capacitance performance of the electrode material in the line with eqn (1). Thereby, this work clearly demonstrates different samples capacitance characteristics under the same condition. Especially, NiS$_2$ with 20 wt% of GO (20%-NiS$_2$/GO) and NiSe$_2$ with 3 wt% of rGO (3%-NiSe$_2$/rGO) show the higher integrated area, implying the higher specific capacitance, while the other composites exhibit the worse pseudo-capacitance among these materials.

To further evaluate the electrochemical performances of these products, GCD tests at different current densities are conducted as shown in Fig. S8 and S9.† In order to make a striking contrast, Fig. 4(c) and (d) shows the discharge profiles
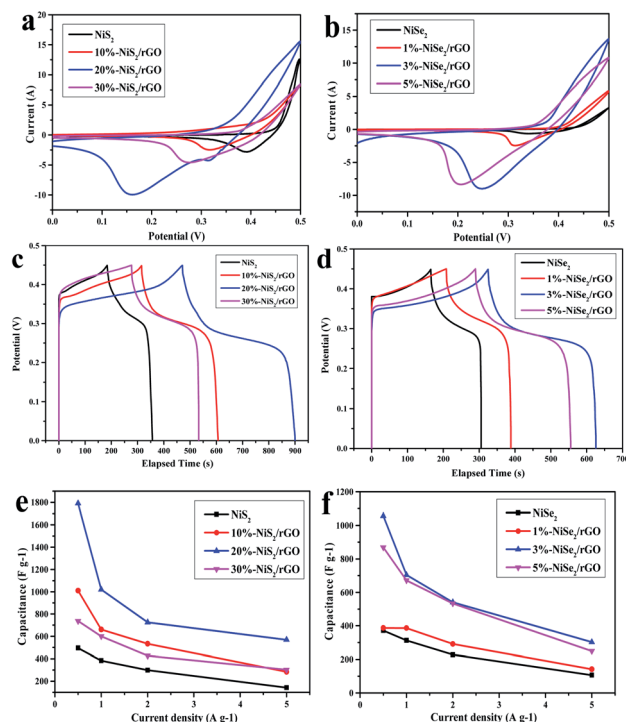
Fig. 4 (a) and (b) CV curves of the four electrodes at a scan rate of 10 mV s$^{-1}$; (c) and (d) GCD curves of the four electrodes at a current density of 1 A g$^{-1}$; (e) and (f) specific capacitances of the four electrodes at various current densities.

of the NiS$_2$ and NiSe$_2$ in contrast with their composites respectively at a current density of 1 A g$^{-1}$, which agree well with their CV curves traits. The obvious plateau regions demonstrate faradic behaviors in the GCD curve of these electrodes, which is caused by redox reactions. The specific capacitance calculations display that samples NiS$_2$ and its composites with 10 wt%, 20 wt%, 30 wt% of GO are 384 F g$^{-1}$, 661 F g$^{-1}$, 1020 F g$^{-1}$ and 600 F g$^{-1}$, respectively. 20%-NiS$_2$/GO shows the highest specific capacitance among these products. NiSe$_2$ and its composites with 1 wt%, 3 wt%, 5 wt% of rGO are 333 F g$^{-1}$, 386 F g$^{-1}$, 722 F g$^{-1}$ and 672 F g$^{-1}$, and 3%-NiSe$_2$/rGO is the highest. Moreover, the specific capacities of the NiS$_2$/rGO and NiSe$_2$/rGO composites are calculated at current densities of 0.5, 1, 2 and 5 A g$^{-1}$ according to eqn (2) respectively,[43] and the calculated capacitances of the composites at corresponding current densities are shown in Fig. 4(e) and (f). As the current density is increased to 5 A g$^{-1}$, the specific capacitances of NiS$_2$ and its composites are 142 F g$^{-1}$, 284 F g$^{-1}$, 568 F g$^{-1}$ and 302 F g$^{-1}$, respectively. NiSe$_2$ and its composites are 106 F g$^{-1}$, 142 F g$^{-1}$, 302 F g$^{-1}$ and 248 F g$^{-1}$. And when the current density is decreased to 0.5 A g$^{-1}$, the specific capacitances of NiS$_2$ and its composites increase to 495.56 F g$^{-1}$, 1010 F g$^{-1}$, 1790 F g$^{-1}$ and 737 F g$^{-1}$. NiSe$_2$ and its composites are 371 F g$^{-1}$, 387 F g$^{-1}$, 1056 F g$^{-1}$ and 868 F g$^{-1}$. In conclusion, the specific capacities of the NiS$_2$/GO and NiSe$_2$/rGO composites have an obvious improvement and show conspicuously better electrochemical performances compared with NiS$_2$ and NiSe$_2$, for which the reason is closely related to the combination of NiS$_2$ and GO or NiSe$_2$ and rGO. In addition,

with the increase of current density, the specific capacitance retentions of NiS$_2$, 20%-NiS$_2$/GO, NiSe$_2$ and 3%-NiSe$_2$/rGO are 28.8%, 31.8%, 28.7% and 28.6%. The above results suggest that the composites not only own higher charge storage capacity but also own the higher rate capacity as the raw material. There have been many recent studies on energy density.[44–46] If the energy density level is high, even an overall enhancement of energy performance can be achieved. Among them, the energy density of 20%-NiS$_2$/GO is 28.7 W h kg$^{-1}$ and 3%-NiSe$_2$/rGO is 20.3 W h kg$^{-1}$ at current density of 1 A g$^{-1}$. Fig. S10(a)† shows the cyclic performance of these electrode materials at a current density of 1 A g$^{-1}$ and the voltage range was from 0 V to 0.45 V. The specific capacitance of NiS$_2$ and 20%-NiS$_2$/GO dropped sharply in the first 20 cycles, from 387 F g$^{-1}$ and 1020 F g$^{-1}$ declined to 144 F g$^{-1}$ and 511 F g$^{-1}$, respectively. And the specific capacitance of NiSe$_2$ and 3%-NiSe$_2$/rGO dropped sharply in the first 20 cycles, from 333 F g$^{-1}$ and 722 F g$^{-1}$ declined to 202 F g$^{-1}$ and 378 F g$^{-1}$, respectively. The rapid decrease of specific capacitance may be owing to the transformation of the structure which was caused by the volume expansion and contraction in the process of redox reactions.[47] According to Fig. S10(b)† the retention rates of NiS$_2$, 20%-NiS$_2$/GO, NiSe$_2$ and 3%-NiSe$_2$/rGO were 17.3%, 13.1%, 20% and 18.4% after 100 cycles, respectively. Under the condition that the capacitance retention rate of the composite product is maintained at about the same level, the specific capacitance is greatly improved.

To further illustrate the difference in electrochemical performance between these four materials, we performed an electrochemical impedance spectra (EIS) experiments. Fig. 5 demonstrates the Nyquist plots of the four electrodes to illustrate their impedance characteristics. In general, the Nyquist diagram of electrode materials for redox supercapacitors should include a semicircle related to the Faraday reaction in the high frequency region and a straight line related to the Warburg impedance in the low frequency region.[48] From the equivalent circuit model, it can be seen that the electrode systems contained electrolyte solution resistance ($R_e$), the faradaic charge transfer resistance associated with the electron transfer ($R_{ct}$), Warburg impedance resistance in ions diffusion process ($Z_w$) and the double layer capacitance at the electrode/electrolyte
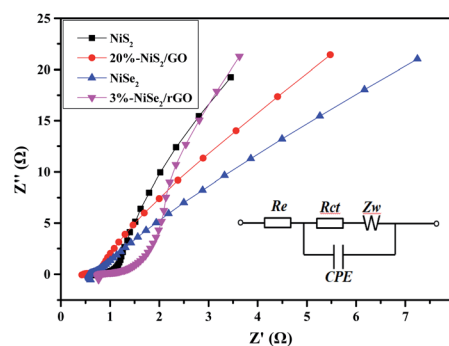


Fig. 5 Nyquist plots of NiS$_2$, 20%-NiS$_2$/GO, NiSe$_2$ and 3%-NiSe$_2$/rGO electrodes, the inset is equivalent circuit model.

interface (CPE).[49] The impedance parameters could be matched by Zview software. The $R_{ct}$ of the $NiS_2$, 20%-$NiS_2$/GO, $NiSe_2$ and 3%-$NiSe_2$/rGO electrodes are 0.29 Ω, 0.11 Ω, 0.66 Ω, 0.22 Ω, respectively. The 20%-$NiS_2$/GO and 3%-$NiSe_2$/rGO electrodes with relatively lower $R_{ct}$ may result from the introduction of carbon material. EIS experiments show that 20%-$NiS_2$/GO and 3%-$NiSe_2$/rGO have lower charge transfer resistance than $NiS_2$ and $NiSe_2$.

# 4 Conclusion

In summary, we have successfully synthesized a carbon-loaded material ($NiS_2$/GO) by introducing graphite oxide with different mass fractions through a L-cysteine-assisted facile hydrothermal method. Meanwhile, during the transformation of $NiS_2$ to $NiSe_2$, graphene oxide was introduced to form $NiSe_2$ composite. The specific capacitance was increased with the addition of graphene oxide and the rate performance were improved. The carbon-loaded layer effectively enhanced the electrical conductivity. Compared with pure $NiS_2$, the specific capacitance of $NiS_2$/GO raised from 384 F $g^{-1}$ to 1020 F $g^{-1}$ at the current density of 1 A $g^{-1}$. And for $NiSe_2$, the specific capacitance of $NiSe_2$/rGO raised from 333 F $g^{-1}$ to 722 F $g^{-1}$ at the current density of 1 A $g^{-1}$. This work demonstrates that the introduction of graphite oxide and carbon-loaded layer was an effective method to improve the overall electrochemical properties of nickel chalcogenide.

## Conflicts of interest

There are no conflicts to declare.

## Acknowledgements

## Notes and references

1 J. Miot, N. Recham, D. Larcher, F. Guyot, J. Brest and J. M. Tarascon, *Energy Environ. Sci.*, 2014, **7**, 451–460.

2 J. Wang, Z. Liu, Y. Zheng, L. Cui, W. Yang and J. Liu, *J. Mater. Chem. A*, 2017, **5**, 22913–22932.

3 R. German, A. Sari, P. Venet, M. Ayadi, O. Briat and J. M. Vinassa, *Microelectron. Reliab.*, 2014, **54**, 1813–1817.

4 Z. Luo, C. Liu and S. Fan, *J. Mater. Chem. A*, 2019, **7**, 3642–3647.

5 C. Yang, D. Li, H. Gao, Q. Liu, J. Zhu, F. Wang and M. Jiang, *ACS Appl. Energy Mater.*, 2020, **3**, 2674–2681.

6 T. Peng, H. Yi, P. Sun, Y. Jing, R. Wang, H. Wang and X. Wang, *J. Mater. Chem. A*, 2016, **4**, 8888–8897.

7 Y. Huang, J. Liang and Y. Chen, *Small*, 2012, **8**, 1805–1834.

8 Y. W. Lee, B. S. Kim, J. Hong, H. Choi, H. S. Jang, B. Hou, S. Pak, J. Lee, S. H. Lee, S. M. Morris, D. Whang, J. P. Hong, H. S. Shin, S. N. Cha, J. I. Sohn and J. M. Kim, *Nano Energy*, 2017, **37**, 15–23.

9 X. Li, S. Y. Lin, M. Zhang, G. Jiang and H. Gao, *Nano*, 2016, **11**, 1650050.

10 X. Chen, R. Paul and L. Dai, *Natl. Sci. Rev.*, 2017, **4**, 453–489.

11 Y. Li, X. Han, T. Yi, Y. He and X. Li, *J. Energy Chem.*, 2018, **31**, 54–78.

12 J. Liu, S. Liu, S. Zhuang, X. Wang and F. Tu, *Ionics*, 2013, **19**, 1255–1261.

13 D. Yan, H. Zhang, S. Li, G. Zhu, Z. Wang, H. Xu and A. Yu, *J. Alloys Compd.*, 2014, **607**, 245–250.

14 G. C. Li, P. F. Liu, R. Liu, M. Liu, K. Tao, S. R. Zhu, M. K. Wu, F. Y. Yi and L. Han, *Dalton Trans.*, 2016, **45**, 13311–13316.

15 J. Yang, M. Cho and Y. Lee, *Sens. Actuators, B*, 2016, **222**, 674–681.

16 M. S. Kolathodi, M. Palei and T. S. Natarajan, *J. Mater. Chem. A*, 2015, **3**, 7513–7522.

17 H. Pang, Q. Lu, Y. Zhang, Y. Li and F. Gao, *Nanoscale*, 2010, **2**, 920–922.

18 R. Sun, S. Liu, Q. Wei, J. Sheng, S. Zhu, Q. An and L. Mai, *Small*, 2017, **13**, 1701744.

19 A. Mondal, S. Maiti, S. Mahanty and A. B. Panda, *J. Mater. Chem. A*, 2017, **5**, 16854–16864.

20 X. Li, J. Shen, N. Li and M. Ye, *Mater. Lett.*, 2015, **139**, 81–85.

21 M. Hua, S. Zhang, B. Pan, W. Zhang, L. Lv and Q. Zhang, *J. Hazard. Mater.*, 2012, **211**, 317–331.

22 C. Wei, C. Cheng, Y. Cheng, Y. Wang, Y. Xu, W. Du and H. Pang, *Dalton Trans.*, 2015, **44**, 17278–17285.

23 J. Wang, S. Dong, B. Ding, Y. Wang, X. Hao, H. Dou, Y. Xia and X. Zhang, *Natl. Sci. Rev.*, 2017, **4**, 71–90.

24 X. Li, J. Shen, N. Li and M. Ye, *Mater. Lett.*, 2015, **139**, 81–85.

25 F. Cai, R. Sun, Y. Kang, H. Chen, M. Chen and Q. Li, *RSC Adv.*, 2015, **5**, 23073–23079.

26 R. Agrawal, C. Chen, Y. Hao, Y. Song and C. Wang, *Graphene-Based Energy Devices*, Wiley-VCH, Weinheim, 2015.

27 L. Wang, X. Wang, X. Xiao, F. Xu, Y. Sun and Z. Li, *Electrochim. Acta*, 2013, **111**, 937–945.

28 H. Zhang, X. Tian, C. Wang, H. Luo, J. Hu, Y. Shen and A. Xie, *Appl. Surf. Sci.*, 2014, **314**, 228–232.

29 I. Oh, M. Kim and J. Kim, *Appl. Surf. Sci.*, 2015, **328**, 222–228.

30 Q. Wang, Y. Zou, C. Xiang, H. Chu, H. Zhang, F. Xu, L. Sun and C. Tang, *Ceram. Int.*, 2016, **42**, 12129–12135.

31 Q. Chen, W. Chen, J. Ye, Z. Wang and J. Y. Lee, *J. Power Sources*, 2015, **294**, 51–58.

32 X. Xie, Z. Ao, D. Su, J. Zhang and G. Wang, *Adv. Funct. Mater.*, 2015, **25**, 1393–1403.

33 C. A. Pandey, S. Ravuri, R. Ramachandran, R. Santhosh, S. Ghosh, S. R. Sitaraman and A. N. Grace, *Int. J. Nanosci.*, 2018, **17**, 1760021.

34 J. Shen, R. Cheng, Y. Luo, Y. Chen, X. Chen, Z. Sun and S. Huang, *J. Solid State Electrochem.*, 2015, **19**, 1045–1052.

35 J. Zhu, Y. Li, S. Kang, X. L. Wei and P. K. Shen, *J. Mater. Chem. A*, 2014, **2**, 3142–3147.

36 W. Ma, Y. Guo, X. Liu, D. Zhang, T. Liu, R. Ma, K. Zhou and G. Qiu, *Chem.–Eur. J.*, 2013, **19**, 15467–15471.

37 M. Lu, X. P. Yuan, X. H. Guan and G. S. Wang, *J. Mater. Chem. A*, 2017, **5**, 3621–3627.

38 F. Zheng, M. Guo and M. Zhang, *CrystEngComm*, 2013, **15**, 277–284.

39 X. H. Guan, Z. W. Zhang, L. Yang and G. S. Wang, *ChemPlusChem*, 2017, **82**, 1174–1181.

40 U. M. Patil, K. V. Gurav, V. J. Fulari, C. D. Lokhande and O. S. Joo, *J. Power Sources*, 2019, **188**, 338–342.

41 K. Chang and W. Chen, *ACS Nano*, 2011, **5**, 4720–4728.

42 Z. Ma, H. Zhang, Y. Zhang, J. Zhang and Z. Li, *Electrochim. Acta*, 2015, **176**, 1427–1433.

43 R. A. Patil, C. P. Chang, R. S. Devan, Y. Liou and Y. R. Ma, *ACS Appl. Mater. Interfaces*, 2016, **8**, 9872–9880.

44 J. J. Yan, L. Miao, H. Duan, D. Z. Zhang, Y. K. Lv, W. Xiong, L. C. Li, L. H. Gan and M. X. Liu, *Electrochim. Acta*, 2020, **358**, 136899.

45 L. Miao, Z. Song, D. Zhu, L. Li, L. Gan and M. Liu, *Mater. Adv.*, 2020, **1**, 945–966.

46 L. Miao, H. Duan, D. Zhu, Y. Lv, L. Gan, L. Li and M. Liu, *J. Mater. Chem. A*, 2021, **9**, 2714–2724.

47 Y. F. Yuan, X. H. Xi, J. B. Wu, J. L. Yang, Y. B. Chen and S. Y. Guo, *Electrochim. Acta*, 2011, **56**, 2627–2632.

48 Y. Li, J. Xu, H. Liu, Y. Liu, M. Wang, J. Li and H. Cui, *J. Sol-Gel Sci. Technol.*, 2018, **87**, 546–553.

49 Yan-qun Liu, Progress on Preparation of Antimony Sulfide Nanomaterialsand Their Applications, *Journal Of Northeast Electric Power University*, 2018, **38**(1), 0082–0087, DOI: 10.19718/j.issn.1005-2992.2018.01.012.